

Effective Bayesian ranking of low order monomial potentials in low temperature warm inflation

Xin Peng¹, Xiang Cheng², Wei Cheng^{*1}, Yi-Rong Ma^{*1}, Pan Yu^{*1}, and Jun Zeng^{*3}

¹School of Electronic Science and Engineering, Chongqing University of Posts and Telecommunications, Chongqing 400065, China

²School of Communication and Information Engineering, Chongqing University of Posts and Telecommunications, Chongqing 400065, China

³College of Physics and Electronic Engineering, Hainan Normal University, Haikou 571158, Hainan, China

Abstract

An effective Bayesian evidence ranking is performed for the monomial potentials $V_p(\phi) = \lambda_p \phi^p/p$, with $p = 2, 3, 4$, in low temperature warm inflation with the dissipative coefficient fixed as $\Upsilon = C_\phi T^3/\phi^2$. In cold single field slow roll inflation, these branches are strongly constrained by the observational upper bound on the tensor to scalar ratio $r = \mathcal{P}_T/\mathcal{P}_R$, whereas warm inflation can reduce this tension by enhancing the scalar spectrum. The relevant question is therefore which monomial power is favored once A_s , n_s , $r_{0.05}$, and the viable parameter volume are considered simultaneously. For each branch, the warm background equations including radiation backreaction are solved, and a broadened compressed likelihood for $(A_s, n_s, r_{0.05})$ is integrated over the prior volume to obtain $Z_{\text{eff}}^{(A_s, n_s, r)}$. For $N_* = 55$, $\sigma_r = 0.005$, and structure conditioned priors covering viable warm branches, the quadratic and cubic potentials are disfavored relative to the quartic branch: $\Delta \ln Z_{\text{eff}}(p = 2) = -32.18$, $\Delta \ln Z_{\text{eff}}(p = 3) = -6.99$. This hierarchy is stable under changes in N_* , prior ranges, random seeds, and the r bound treatment. A representative quartic trajectory gives $n_s = 0.96420$, $r_{0.05} = 0.02663$, $Q_* = 4.68 \times 10^{-3}$, and $T_*/H_* = 10.67$, corresponding to a weakly dissipative but thermally occupied CMB window. Decomposing the primordial spectrum shows that the quartic preference is driven mainly by Bose Einstein occupation enhancement for $T_*/H_* > 1$, not by strong dissipative friction. Within the low temperature dissipative effective class and compressed likelihood adopted here, the evidence hierarchy is $p = 4 > p = 3 \gg p = 2$.

*Corresponding authors. Email: chengwei@cqupt.edu.cn, mayr@cqupt.edu.cn, panyu@cqupt.edu.cn, zengj@hainnu.edu.cn

Contents

1	Introduction	3
2	Theoretical Model and Analytic Cold Inflation	5
2.1	Low order monomial potential	5
2.2	Analytic solution for cold inflation	6
2.3	Low temperature dissipation	7
3	Warm Background Evolution, Primordial Spectrum, and Compressed Likelihood	8
3.1	Warm Background Equations	8
3.2	Primordial Perturbation Spectrum in Warm Inflation	9
3.3	Observable Calculation	11
3.4	Compressed Observable Likelihood and Effective Bayesian Evidence	12
4	Numerical Strategy, Prior Settings, and Evidence Calculation	15
4.1	Computational Procedure	15
4.2	Parameter Space and Structural Conditional Prior	15
4.3	Global Search, Posterior Diagnostics, and Evidence Integration	17
5	Numerical Results and Robustness Analysis	18
5.1	Representative high likelihood Trajectories and the $n_s - r_{0.05}$ Plane	19
5.2	Effective Evidence Ranking and Robustness Tests	19
5.3	Primordial Spectrum Calculation Stability and Low Temperature Trajectory Validity	22
6	Physical Discussion	25
6.1	Physical mechanism favoring the quartic potential	25
6.2	Statistical meaning of the effective evidence	26
6.3	Prior Fairness and Microphysical Cost	26
7	Conclusion	27
A	Structural Conditional Prior Ranges and Sensitivity Settings	29

1. Introduction

Inflation provides a dynamical explanation for the origin of the large scale homogeneity, flatness, and nearly scale invariant curvature perturbations of the universe [1–5]. In the minimal cold single field framework, the inflaton is assumed to remain approximately isolated from other degrees of freedom during the accelerated expansion phase, while scalar perturbations are generated predominantly from quantum fluctuations on a quasi-de Sitter background [6–9]. The corresponding observational predictions are conventionally characterized by the scalar amplitude (A_s), the scalar spectral index (n_s), and the tensor to scalar ratio (r). Constraints from the Planck 2018 inflation analysis yield $n_s = 0.9649 \pm 0.0042$ (68% CL), while the commonly adopted bound from the BICEP/Keck 2018 analysis gives $r_{0.05} < 0.036$ (95% CL) [10–13].

Monomial potentials $V(\phi) \propto \phi^p$, originally motivated by chaotic inflation and subsequent effective field theory considerations, continue to serve as important benchmark models in inflationary cosmology [14–18]. Simple analytic relations are obtained among the power p , the pivot e-fold number N_* , n_s , and r , while these models may also be interpreted as low order operators in an effective scalar potential. Owing to this simplicity, the corresponding observational constraints become particularly transparent. In cold slow roll inflation, r increases with the monomial power p ; consequently, for $N_* \simeq 50$ –60, the quartic potential generally predicts values of r significantly above the current observational upper bound. This difficulty does not correspond merely to a single point fitting issue, but instead reflects a structural limitation arising from the direct connection between the tensor amplitude and the slope of the potential within the cold inflationary background.

Warm inflation modifies the above relations by allowing the inflaton to dissipate energy continuously into a light thermal bath during the inflationary era [19–22]. At the background level, the dissipative term $\Upsilon \dot{\phi}$ increases the effective friction acting on the inflaton and continuously generates radiation, while at the perturbative level the scalar spectrum is enhanced through the combined effects of thermal fluctuations, Bose Einstein occupation numbers, and dissipative growth in the coupled inflaton radiation perturbation system [23–26]. Since the tensor spectrum does not receive an analogous thermal enhancement, warm dynamics can reduce $r = \mathcal{P}_T/\mathcal{P}_R$ through amplification of the scalar spectrum, thereby breaking the simple cold inflation relation $r = 16\epsilon_V$. Recent investigations of warm Higgs inflation and Palatini/ R^2 extensions further demonstrate that thermal dissipation can shift the (n_s, r) predictions in plateau or quartic type potential backgrounds and restore compatibility with CMB observations [27, 28]. In addition, a systematic analysis of the dissipation strength in warm Higgs inflation indicates that the CMB compatible parameter region may naturally arise within the weakly dissipative warm inflation regime characterized by $Q \ll 1$ [29].

The low temperature dissipative coefficient possesses a clear effective theoretic interpretation. In the commonly adopted two stage low temperature mechanism, the dissipative coefficient takes the form $\Upsilon(\phi, T) = C_\phi T^3/\phi^2$ when the thermal bath temperature remains below the heavy mediator mass scale [30–33]. The low temperature condition is defined relative to the heavy mediator threshold through $T < m_\chi(\phi)$, while the warm fluctuation condition is characterized by $T/H > 1$. Consequently, a viable parameter window satisfying $H < T < m_\chi$ can naturally emerge. The dimensionless coefficient C_ϕ encodes the combined enhancement associated with heavy mediator fields, light thermal bath degrees of freedom, and multichannel dissipative effects within the low temperature two stage framework. Motivated by this physical picture, the quan-

tities T/H , T/ϕ , Q , and ρ_R/V are evaluated at the pivot scale, throughout the CMB window, and near the end of inflation in order to characterize both the weakly dissipative low temperature regime relevant for perturbation generation and the radiation enhanced stage approached toward the end of inflation.

Warm inflation has been investigated extensively from several complementary perspectives in the literature. In the context of microphysical model building, low temperature two stage dissipative mechanisms, distributed mass models, the Warm Little Inflaton scenario, Minimal Warm Inflation, and recent realizations based on Standard Model gauge interactions have been proposed [32–37]. In connection with CMB constraints, the consistency of warm inflation models with Planck/BICEP observations has been systematically examined [38–41]. For the dissipative coefficient, a variety of temperature dependences and low temperature effective forms have been employed to describe different underlying microphysical channels [33, 42–44]. In studies of monomial warm inflation, the observational viability of potentials of the form $V \propto \phi^p$ has been reconsidered within warm inflationary backgrounds [45, 46]. Furthermore, for scalar perturbations in warm inflation, analytic approximations, numerical solutions of the perturbation equations, and fitted growth factors have been developed, thereby providing the foundation for the primordial spectrum calculation adopted here [23–26, 47]. Collectively, these studies indicate that warm dissipative dynamics can reopen regions of monomial parameter space that are strongly constrained by tensor perturbations in the conventional cold inflation framework. Motivated by these developments, a more focused and directly testable question is considered: when the dissipative structure, background evolution equations, primordial spectrum calculation, and observational likelihood are held fixed, and when each monomial power is assigned a structure conditioned prior calibrated through broad parameter exploration, which of the low order effective potentials with $p = 2, 3, 4$ receives the strongest support once prior volume effects and stability diagnostics are consistently taken into account?

The monomial potentials $V_p(\phi) = \lambda_p \phi^p/p$, with $p = 2, 3, 4$, are investigated within the low temperature dissipative framework characterized by $\Upsilon = C_\phi T^3/\phi^2$. The cubic potential is treated only as a local effective branch in the positive field region. The analysis is not limited to the identification of isolated viable parameter points; instead, both the best fit regions and the effective Bayesian evidence under the observational likelihood are examined, while the stability of the resulting hierarchy is tested against variations in N_* , prior selections, independent random seeds, and the treatment of the primordial spectral components. Observable deviations in n_s or r already emerge for the quadratic and cubic potentials within the high likelihood region. Through prior averaging, these deviations are further translated into a hierarchy among the monomial branches at the level of effective evidence. In this manner, the conventional tensor to scalar ratio tension associated with cold monomial inflation is reformulated as a controlled ranking problem within a fixed low temperature dissipative effective class¹.

To ensure meaningful comparison of ranking hierarchies, the analysis of the three monomial powers is performed with identical warm inflation background equations, primordial perturbation spectra, and broadened compressed likelihood. The reference prior is fixed through broad parameter exploration together with the identification of viable warm inflation branches, while two additional prior choices are introduced to examine the impact of prior volume effects. The

¹The low temperature dissipative effective class considered here corresponds to a set of warm inflation effective models in which the dissipative coefficient is specified by $\Upsilon(\phi, T) = C_\phi T^3/\phi^2$ within the low temperature two stage mechanism, while the CMB window is required to satisfy $H < T < m_\chi$.

validity of the low temperature effective description is verified explicitly through the conditions $T < m_\chi$, $T/H > 1$, radiation subdominance, and the thermalization window. The CMB window is distinguished from the late stage radiation enhancement regime in order to clarify the dynamical behavior at different stages of inflationary evolution. Furthermore, standard variations in the primordial spectrum calculation, together with an additional test in which the thermal occupation factor is removed, are employed to identify the dominant physical mechanism responsible for the recovery of the quartic potential.

The remainder of the paper is organized as follows. Sec. 2 introduces the low order monomial potentials, the analytic benchmark of cold inflation, and the low temperature dissipative effective description. Sec. 3 presents the warm inflation background equations, the primordial perturbation spectrum, the procedure used for computing observables, and the broadened compressed observable likelihood. Sec. 4 describes the computational framework, parameter space, structure conditioned priors, posterior diagnostics, and nested sampling evidence integration. The main results, including representative high likelihood trajectories, the effective evidence hierarchy, robustness tests, stability analyses of the primordial spectrum calculation, and validity checks of the low temperature trajectories, are presented in Sec. 5. In Sec. 6, the physical mechanism underlying the preference for the quartic potential, together with the statistical interpretation of the effective evidence, issues of prior fairness, and the associated microphysical cost, are discussed. Finally, the main conclusions are summarized in Sec. 7.

2. Theoretical Model and Analytic Cold Inflation

2.1. Low order monomial potential

Throughout the main text, the potential is written in the unified form

$$V_p(\phi) = \frac{\lambda_p}{p} \phi^p, \quad p = 2, 3, 4. \quad (1)$$

Eq. (1) defines the common potential employed in the calculations of the background evolution, the cold inflation benchmark, and the warm inflation primordial spectrum. In reduced Planck units, the potential V carries mass dimension four, whereas the coupling λ_p has mass dimension $4 - p$. The cases $p = 2$ and $p = 4$ correspond to the standard quadratic mass term and quartic self-interaction, respectively. The cubic case ($p = 3$) is included only as a local effective branch in the positive field region, $\phi > 0$. A globally stable completion of this branch would generally require additional stabilizing operators or an explicitly specified symmetry breaking mechanism. Consequently, the $p = 3$ branch considered here is interpreted as a low order expansion of an underlying stable potential over the positive field CMB regime, rather than as a globally complete scalar potential. More generally, the effective potential may contain higher order stabilizing contributions, for example $V = V_0 + a_2\varphi^2 + a_3\varphi^3 + a_4\varphi^4 + \dots$. Provided that these higher order operators remain subdominant throughout the CMB field range considered here, the cubic branch may be treated as a controlled local effective model. Under this interpretation, the unbounded behavior associated with the isolated cubic term in the negative field region does not affect the physical conclusions derived below.

2.2. Analytic solution for cold inflation

For $V \propto \phi^p$, the cold slow roll parameters are

$$\epsilon_V = \frac{1}{2} \left(\frac{V_{,\phi}}{V} \right)^2 = \frac{p^2}{2\phi^2}, \quad \eta_V = \frac{V_{,\phi\phi}}{V} = \frac{p(p-1)}{\phi^2}. \quad (2)$$

where $V_{,\phi} \equiv dV/d\phi$ and $V_{,\phi\phi} \equiv d^2V/d\phi^2$ denote the first and second derivatives of the potential V with respect to the scalar field ϕ , respectively. The ratios $V_{,\phi}/V$ and $V_{,\phi\phi}/V$ characterize the relative slope and curvature of the potential, respectively, and thus provide dimensionless measures of the flatness of the inflationary potential relevant for slow roll evolution. Throughout this work, the same comma notation is adopted to denote derivatives with respect to the scalar field ϕ .

The condition for the end of cold slow roll inflation is $\epsilon_V(\phi_{\text{end}}) = 1$, hence $\phi_{\text{end}} = p/\sqrt{2}$. The pivot field value satisfies

$$N_* \simeq \int_{\phi_{\text{end}}}^{\phi_*} \frac{V}{V_{,\phi}} d\phi = \frac{\phi_*^2 - \phi_{\text{end}}^2}{2p}, \quad \phi_*^2 = 2pN_* + \frac{p^2}{2}. \quad (3)$$

Here and throughout the paper, the subscript $*$ denotes quantities evaluated at horizon crossing of the pivot scale $k_* = 0.05 \text{ Mpc}^{-1}$. Hence, the cold slow roll parameters can be derived

$$\epsilon_{V,*} = \frac{p}{4N_* + p}, \quad \eta_{V,*} = \frac{2(p-1)}{4N_* + p}. \quad (4)$$

The first order slow roll relations in cold inflation are

$$n_s^{\text{cold}} - 1 = -6\epsilon_{V,*} + 2\eta_{V,*}, \quad r^{\text{cold}} = 16\epsilon_{V,*}. \quad (5)$$

Substituting the slow roll parameters yields

$$n_s^{\text{cold}} = 1 - \frac{2(p+2)}{4N_* + p}, \quad r^{\text{cold}} = \frac{16p}{4N_* + p}. \quad (6)$$

For $N_* = 55$, the cold inflation benchmark results are listed in Tab. 1. These results are included solely for reference purposes and are not incorporated into the effective evidence ranking of the warm inflation models.

Table 1: Analytic benchmark for cold monomial potentials with $N_* = 55$. The last column gives the qualitative assessment relative to the current n_s and $r_{0.05}$ constraints.

Model	N_*	ϕ_*	$\epsilon_{V,*}$	n_s^{cold}	r^{cold}	Qualitative interpretation
$p = 2$	55	14.8997	0.0090	0.9640	0.1441	n_s is close to the observational central values, but r is clearly too large.
$p = 3$	55	18.2893	0.0135	0.9552	0.2152	n_s is on the low side, and r is even larger than for the quadratic potential.
$p = 4$	55	21.1660	0.0179	0.9464	0.2857	n_s is further on the low side, and r is the largest.

2.3. Low temperature dissipation

The warm model adopts the low temperature dissipative form

$$\Upsilon(\phi, T) = C_\phi \frac{T^3}{\phi^2}. \quad (7)$$

where C_ϕ denotes the dimensionless effective dissipation strength that parametrizes the cumulative contribution of multiple degrees of freedom and composite interaction channels within the low temperature two stage dissipative mechanism [30, 31, 33]. When the heavy mediator mass is expressed as $m_\chi(\phi) = g_\chi \phi$, the validity of the low temperature expansion requires

$$T < m_\chi, \quad \text{conservatively written as} \quad g_\chi > \frac{T}{\phi}. \quad (8)$$

If the thermalization rate of the light thermal bath is parameterized as $\Gamma_{\text{th}} = \kappa T$, the condition for efficient thermalization may be expressed as

$$\frac{\Gamma_{\text{th}}}{H} > 1, \quad \kappa > \frac{H}{T}. \quad (9)$$

These conditions are verified individually at the pivot scale and across different e-fold intervals. Unless stated otherwise, the numerical analysis adopts $g_* = 228.75$ as the benchmark effective number of relativistic degrees of freedom corresponding to a supersymmetric-like thermal bath. Although this choice does not represent a unique microscopic realization, it provides a representative benchmark within the low temperature dissipative effective class considered here. The quantities g_* and C_ϕ play distinct physical roles: g_* characterizes the light degrees of freedom that remain relativistic within the thermal bath, whereas C_ϕ parametrizes the effective strength of the low temperature dissipative channel. The latter may be enhanced by the multiplicity of heavy mediator fields, the coupling structure of the light sector, and the presence of a composite dissipative sector.

Since

$$\frac{m_\chi}{H} = g_\chi \frac{\phi}{H} = g_\chi \frac{T/H}{T/\phi}, \quad (10)$$

It is found that, within the CMB window, $T/H \sim 10$ and $T/\phi \sim 10^{-5}$, which implies $\phi/H \sim 10^6$. Consequently, the conditions $T < m_\chi$ and $m_\chi \gg H$ can be simultaneously satisfied even for moderately small values of g_χ . Under these circumstances, the heavy mediator field may consistently be integrated out within the effective description. The coefficient C_ϕ is therefore treated as an effective parameter arising from enhancements associated with multiple degrees of freedom or composite dissipative channels, rather than as a single elementary coupling constant. Its large numerical value constitutes the principal microphysical cost of the realization considered here, while an explicit microscopic implementation is deferred to a more complete construction of the dissipative sector.

3. Warm Background Evolution, Primordial Spectrum, and Compressed Likelihood

3.1. Warm Background Equations

The background dynamics of warm inflation are governed collectively by the inflaton field, the radiation bath, and the Friedmann constraint. The background evolution equations are given by

$$\ddot{\phi} + (3H + \Upsilon)\dot{\phi} + V_{,\phi} = 0, \quad (11)$$

$$\dot{\rho}_R + 4H\rho_R = \Upsilon\dot{\phi}^2, \quad (12)$$

$$H^2 = \frac{1}{3M_{\text{Pl}}^2} \left(\frac{1}{2}\dot{\phi}^2 + V + \rho_R \right). \quad (13)$$

where $H = \dot{a}/a$. In Eq. (11), the term $3H\dot{\phi}$ corresponds to the Hubble friction, while $\Upsilon\dot{\phi}$ represents the dissipative friction contribution; both terms act to slow the evolution of the inflaton along the potential. Eq. (12) governs the evolution of the radiation energy density, where $4H\rho_R$ describes the dilution of radiation due to cosmic expansion and $\Upsilon\dot{\phi}^2$ denotes the source term through which inflaton kinetic energy is transferred into radiation via dissipation. Eq. (13) provides the Friedmann constraint relating the total energy density to the cosmic expansion rate. Throughout this work, an overdot stands for differentiation with respect to cosmic time, i.e., $\dot{X} \equiv dX/dt$.

The radiation energy density is related to the temperature through

$$\rho_R = \frac{\pi^2}{30} g_* T^4. \quad (14)$$

The principal results presented here are obtained with $g_* = 228.75$. This choice affects the relation between T and ρ_R , and should therefore be regarded as a reference specification for the effective number of thermal bath degrees of freedom. Physically, g_* counts the relativistic light degrees of freedom within the thermal bath, whereas C_ϕ may additionally encode enhancements arising from integrated-out heavy mediators, multiple dissipative channels, or composite dissipative sectors. Consequently, no one-to-one correspondence between g_* and C_ϕ is required within the effective description adopted here. A complete microscopic realization would instead require an explicit specification of the underlying particle spectrum. Combined with the low temperature dissipative coefficient $\Upsilon = C_\phi T^3/\phi^2$, Eq. (14) further implies that Υ should not be regarded as an externally fixed constant, but rather as a background dependent quantity determined jointly by ϕ and ρ_R .

The strength of dissipation is conventionally characterized by the dimensionless ratio

$$Q \equiv \frac{\Upsilon}{3H}, \quad (15)$$

The condition $Q \ll 1$ indicates that the background evolution remains primarily controlled by Hubble friction, whereas $Q \gtrsim 1$ signifies that dissipative friction exerts a dominant influence on the rolling dynamics of the inflaton. The numerical trajectory analysis presented below further shows that the CMB window is located within the weak dissipation regime, while the final stage of inflation may evolve toward a radiation enhanced phase.

The Hubble slow roll parameter may be expressed directly from energy conservation as

$$\dot{H} = -\frac{1}{2M_{\text{Pl}}^2} \left(\dot{\phi}^2 + \frac{4}{3}\rho_R \right), \quad \epsilon_H \equiv -\frac{\dot{H}}{H^2} = \frac{\dot{\phi}^2 + 4\rho_R/3}{2M_{\text{Pl}}^2 H^2}. \quad (16)$$

Consequently, the condition for accelerated expansion is given by $\epsilon_H < 1$, while the end of inflation is defined by $\epsilon_H = 1$. This criterion explicitly incorporates the contribution of the radiation energy density to \dot{H} , and is therefore more appropriate for warm inflationary backgrounds than a description based solely on the potential slow roll parameter.

In the numerical analysis, the e-fold number $N \equiv \ln a$ is adopted as the time variable. By defining $\pi_\phi \equiv \dot{\phi}$ and using the relation $d/dt = Hd/dN$, Eqs. (11)–(12) may be rewritten in first order form as

$$\frac{d\phi}{dN} = \frac{\pi_\phi}{H}, \quad (17)$$

$$\frac{d\pi_\phi}{dN} = -\frac{(3H + \Upsilon)\pi_\phi + V_{,\phi}}{H}, \quad (18)$$

$$\frac{d \ln \rho_R}{dN} = -4 + \frac{\Upsilon \pi_\phi^2}{H \rho_R}. \quad (19)$$

The third equation is written in terms of $\ln \rho_R$ in order to preserve the positivity of the radiation energy density and to improve numerical stability when ρ_R spans multiple orders of magnitude. At each integration step, the temperature T is determined from Eq. (14), the dissipative coefficient Υ is obtained from Eq. (7), and the Hubble expansion rate H is evaluated through the Friedmann Eq. (13), thereby yielding a closed system for the background evolution.

In the slow roll regime with subdominant radiation energy density, the full background equations reduce to the standard warm inflation slow roll relations:

$$3H(1+Q)\dot{\phi} \simeq -V_{,\phi}, \quad 4H\rho_R \simeq \Upsilon\dot{\phi}^2, \quad H^2 \simeq \frac{V}{3M_{\text{Pl}}^2}. \quad (20)$$

These relations provide a useful physical interpretation of warm inflation: the dissipative friction suppresses $|\dot{\phi}|$ through the factor $1+Q$, while the source term $\Upsilon\dot{\phi}^2$ continuously maintains the thermal radiation bath. Nevertheless, the numerical results presented here are not based on the analytic approximation of Eq. (20), but are instead obtained through direct numerical integration of the background Eqs. (17)–(19). The location of the pivot scale is specified by the reference condition $N_{\text{end}} - N_* = 55$, and the stability of the results is further examined for $N_* = 50, 55, 60$.

3.2. Primordial Perturbation Spectrum in Warm Inflation

The scalar perturbations in warm inflation differ fundamentally from the pure vacuum fluctuations characteristic of cold inflation. Owing to the interaction between the inflaton field and the thermal bath, the curvature perturbation receives simultaneous contributions from three distinct sources: vacuum fluctuations on a quasi-de Sitter background, thermal occupation effects generated by the thermal bath, and dissipative growth associated with the coupling between

inflaton and radiation perturbations. The scalar power spectrum adopted here is given by [23–26]

$$\mathcal{P}_{\mathcal{R}}(k_*) = \left(\frac{H_*^2}{2\pi|\dot{\phi}_*|} \right)^2 \left[1 + 2n_* + \frac{2\sqrt{3}\pi Q_*}{\sqrt{3+4\pi Q_*}} \frac{T_*}{H_*} \right] G(Q_*), \quad (21)$$

where the prefactor corresponds to the standard vacuum contribution to the curvature power spectrum in cold inflation. Within the square brackets, the term 1 represents the vacuum contribution, $2n_*$ describes the enhancement arising from the initial thermal occupation number, and the final term accounts for the combined effects of thermal noise and dissipative coupling on the inflaton fluctuations. The thermal occupation number is assumed to follow the Bose Einstein distribution:

$$n_* = \frac{1}{\exp(H_*/T_*) - 1}. \quad (22)$$

When $T_*/H_* > 1$, the occupation number n_* can no longer be neglected, and the scalar spectrum may become significantly enhanced relative to the vacuum spectrum of cold inflation. In particular, in the limit $T_*/H_* \gg 1$,

$$n_* \simeq \frac{T_*}{H_*}, \quad 1 + 2n_* \simeq 1 + 2\frac{T_*}{H_*}. \quad (23)$$

For the representative quartic trajectory, $T_*/H_* = 10.67$, so the thermal occupation term provides an order of magnitude enhancement of the scalar spectrum. As a result, the tensor to scalar ratio

$$r = \mathcal{P}_T/\mathcal{P}_{\mathcal{R}}$$

is significantly reduced relative to the corresponding cold inflation expectation.

Equation (22) should not be interpreted as an identity derived from the background dynamics. It is a thermal occupation assumption: the inflaton fluctuations are assumed to acquire an approximately thermal distribution through interactions with the radiation bath before horizon crossing. The model ranking obtained in this work therefore relies on this assumption. In a later test, the choice $n_* = 0$ is imposed to represent the limiting case in which the inflaton fluctuations do not acquire a Bose Einstein thermal occupation. This comparison is used to quantify the importance of the thermal occupation contribution to the scalar spectrum.

The function $G(Q)$ characterizes the growth effect induced by the coupling between inflaton and radiation perturbations. It is not an additional free function, but an empirical fitting factor extracted from numerical solutions of the warm inflation perturbation equations. This type of fitting factor has been widely used in analyses of warm inflation perturbation spectra and CMB constraints [22, 26, 34, 39]. For a dissipative coefficient with cubic temperature dependence, a commonly used fitting form is

$$G_{\text{cubic}}(Q_*) = 1 + 4.981 Q_*^{1.946} + 0.127 Q_*^{4.330}. \quad (24)$$

This fitting expression summarizes the numerical growth effect from the coupled perturbation equations in the case $\Upsilon \propto T^3$ [26, 48, 49]. The fitting coefficients depend on the temperature dependence of the dissipative coefficient. For example, in the case of linear temperature dependence, a commonly adopted fitting form is [22]

$$G_{\text{linear}}(Q_*) = 1 + 0.335 Q_*^{1.364} + 0.0185 Q_*^{2.315}. \quad (25)$$

The low temperature dissipative mechanism considered here belongs to the class with cubic temperature dependence, and Eq. (24) is therefore adopted as the baseline growth factor throughout the analysis. The same fitting form is implemented in the numerical calculation to keep the primordial spectrum setup consistent with the analytic description. At the best-fit point and throughout the CMB window explored in this work, the dissipation strength remains at the level $Q \sim 10^{-3}$, for which the commonly used fitting forms give $G(Q) \simeq 1$. Consequently, the influence of the growth factor on the effective model ranking is substantially weaker than that of the thermal occupation contribution. In subsequent tests, the different components of the primordial scalar spectrum are examined by varying the strength of $G(Q)$, setting $G(Q) = 1$, and considering the limiting case $n_* = 0$.

The tensor perturbations do not directly receive the same thermal enhancement from the radiation bath, and their spectrum therefore retains the standard form:

$$\mathcal{P}_T(k_*) = \frac{2H_*^2}{\pi^2 M_{\text{Pl}}^2}, \quad r_{0.05} = \frac{\mathcal{P}_T(k_*)}{\mathcal{P}_{\mathcal{R}}(k_*)}. \quad (26)$$

The modification of the tensor-to-scalar ratio in warm inflation arises predominantly from the enhancement of the scalar spectrum $\mathcal{P}_{\mathcal{R}}$, rather than from any direct suppression of the tensor spectrum itself. This feature plays a central role in understanding the recovery of the quartic branch in the warm inflation background. The scalar amplitude and spectral index are evaluated from the same background trajectory, as described in Sec. 3.3.

3.3. Observable Calculation

For a given monomial power p and parameter set θ , the observables are evaluated according to the following procedure. The background system defined by Eqs. (11)–(13) is first solved numerically, while the end of inflation is determined through the condition $\epsilon_H = 1$. The pivot point associated with a specified value of N_* is subsequently identified by moving backward from the end of inflation. At this pivot scale, the quantities H_* , $\dot{\phi}_*$, Q_* , T_* , and $\rho_{R,*}$ are extracted from the numerical trajectory. The scalar amplitude is then defined as

$$A_s = \mathcal{P}_{\mathcal{R}}(k_*), \quad (27)$$

where $\mathcal{P}_{\mathcal{R}}$ is given by Eq. (21). The scalar spectral index is defined by

$$n_s - 1 = \left. \frac{d \ln \mathcal{P}_{\mathcal{R}}}{d \ln k} \right|_{k_*}. \quad (28)$$

Using the horizon-crossing relation $k = aH$, one has

$$d \ln k = d \ln(aH) = (1 - \epsilon_H) dN, \quad (29)$$

where $N \equiv \ln a$ denotes the forward e-fold integration variable. To avoid ambiguity between this forward variable and the remaining number of e-folds before the end of inflation, the forward pivot position is defined as

$$N_{\text{piv}} = N_{\text{end}} - N_*, \quad N_{\pm} = N_{\text{piv}} \pm \Delta N, \quad (30)$$

where the quantity N_* appearing in the results tables represents the number of remaining e-folds between the pivot scale and the end of inflation.

In the numerical implementation, $\ln \mathcal{P}_{\mathcal{R}}$ is evaluated along the same background trajectory at N_- , N_{piv} , and N_+ , with $\Delta N = 0.20$. These three values are obtained by shifting the horizon-crossing position along the forward variable $N = \ln a$, reevaluating H , $\dot{\phi}$, Q , T , and ρ_R , and substituting these quantities into Eq. (21). A local quadratic fit of $\ln \mathcal{P}_{\mathcal{R}}$ as a function of $N - N_{\text{piv}}$ is then used to extract

$$\left. \frac{d \ln \mathcal{P}_{\mathcal{R}}}{dN} \right|_*. \quad (31)$$

The scalar spectral index is finally computed through the local horizon-crossing conversion:

$$n_s - 1 \simeq \frac{1}{1 - \epsilon_{H,*}} \left. \frac{d \ln \mathcal{P}_{\mathcal{R}}}{dN} \right|_*. \quad (32)$$

Equation (32) is the numerical procedure adopted in this work. It keeps the leading correction from the variation of H through the factor $1 - \epsilon_{H,*}$, rather than approximating $d \ln k$ simply by dN . The quantities $\mathcal{P}_{\mathcal{R}}(N_{\pm})$ are therefore not independently adjusted amplitudes; they are computed from the same warm-inflation trajectory by shifting the pivot location and reevaluating the local background quantities. If the remaining e-fold variable

$$N_{\text{to end}} = N_{\text{end}} - N$$

were adopted instead, an additional minus sign would appear in the derivative relation. Both the numerical implementation and the notation used here are formulated in terms of the forward variable N . The sensitivity of the results to variations in ΔN is included as part of the stability analysis of the primordial spectrum calculation.

The tensor spectrum is evaluated using Eq. (26). Consequently, the observables A_s , n_s , and $r_{0.05}$ are all determined self-consistently from the same warm inflation background trajectory, rather than being adjusted independently.

3.4. Compressed Observable Likelihood and Effective Bayesian Evidence

The likelihood employed in this work is a broadened compressed likelihood constructed from the three pivot scale observables A_s , n_s , and $r_{0.05}$ [50, 51]. This likelihood is applied directly to the observables A_s , n_s , and $r_{0.05}$. For each parameter set θ and each specified monomial power p , the pivot scale quantities H_* , $\dot{\phi}_*$, Q_* , and T_* are first obtained from the warm inflation background equations. The corresponding theoretical prediction for the observable vector is then computed from Eqs. (21)–(26) as

$$\mu(\theta|p) = (\ln(10^{10} A_s), n_s, r_{0.05}). \quad (33)$$

The likelihood function is therefore determined jointly by the scalar amplitude, the spectral tilt, and the tensor amplitude predicted from the same warm inflation background trajectory.

The scalar amplitude and the scalar spectral index are assumed to follow Gaussian likelihood

distributions:

$$\chi_A^2 = \left[\frac{\ln(10^{10} A_s) - \ln(10^{10} A_s)_{\text{obs}}}{\sigma_A} \right]^2, \quad (34)$$

$$\chi_n^2 = \left[\frac{n_s - n_{s,\text{obs}}}{\sigma_n} \right]^2. \quad (35)$$

The numerical values adopted in the analysis are listed in Tab. 2. Since current observations of r provide primarily an upper bound rather than a two sided measurement around a central value, the r constraint is implemented here through a one sided penalty function:

$$\chi_r^2 = \begin{cases} 0, & r_{0.05} \leq r_{\text{lim}}, \\ [(r_{0.05} - r_{\text{lim}})/\sigma_r]^2, & r_{0.05} > r_{\text{lim}}. \end{cases} \quad (36)$$

This definition implies that parameter points lying below the observational upper bound on r are not assigned additional statistical preference for predicting even smaller values of r , whereas points exceeding the bound receive a continuous likelihood penalty determined by the magnitude of the excess. The parameter σ_r controls the smoothness of the penalty transition near the upper limit. In the reference setup adopted here, $r_{\text{lim}} = 0.036$ and $\sigma_r = 0.005$ are used, such that points lying only slightly above the bound are not abruptly excluded, while points substantially exceeding the limit experience a rapid suppression of their likelihood. Since the best fit quartic solution is located close to the observational upper bound on r , the choice of σ_r represents a potentially important systematic factor in the effective evidence ranking. To test the robustness of the hierarchy against the treatment of the upper limit smoothing, three representative values, $\sigma_r = 0.003, 0.005, 0.010$, are examined in the analysis.

Table 2: The inputs adopted in the broadened compressed observable likelihood. The scalar amplitude uses a conservatively broadened error $\sigma_A = 0.08$, rather than the narrow error from the full Planck posterior; r adopts a one sided upper limit penalty.

Observables	Adopted value or limit	Likelihood treatment
$\ln(10^{10} A_s)$	3.044	Gaussian, $\sigma_A = 0.08$
n_s	0.9649	Gaussian, $\sigma_n = 0.0042$
$r_{0.05}$	< 0.036	One sided penalty, $\sigma_r = 0.005$

In addition to satisfying observational constraints, the inflationary trajectory is also required to remain within the regime of validity of warm inflation. The corresponding overall discriminant function is defined as

$$\chi^2 = \chi_A^2 + \chi_n^2 + \chi_r^2 + \chi_{\text{warm}}^2 + \chi_{\text{phys}}^2, \quad \mathcal{L}_{\text{obs}} = \exp\left(-\frac{1}{2}\chi^2\right). \quad (37)$$

where χ_{warm}^2 imposes the warm inflation condition $T_*/H_* > 1$ at the pivot scale, while χ_{phys}^2 excludes trajectories exhibiting negative radiation density, insufficient inflationary e-folds, violation of the low temperature condition, or failure of the background evolution to reach the end of inflation. For parameter points satisfying these physical requirements, the final two contributions remain either zero or negligibly small; by contrast, trajectories that clearly violate these conditions receive a large penalty, thereby preventing them from contributing significantly to the high likelihood region or to the effective evidence. In this manner, the likelihood function si-

multaneously incorporates both observational consistency and the basic physical viability of the warm inflation background. The quantity \mathcal{L}_{obs} should therefore be interpreted only as the local statistical weight assigned to an individual parameter point, answering the question of whether the trajectory associated with that point is compatible with the observational constraints. It does not itself represent the model evidence. A meaningful comparison between models additionally requires evaluating the total volume of high likelihood trajectories across the full prior parameter space; consequently, \mathcal{L}_{obs} must be integrated over the adopted prior region.

The choice $\sigma_A = 0.08$ adopted in Tab. 2 is consistent with the numerical setup used throughout all principal results presented in this work. If a narrower uncertainty corresponding to the Planck compressed parameters were instead adopted, for example $\sigma_A \simeq 0.014$, a different effective likelihood problem would be defined, and the corresponding evidence would need to be recomputed through a separate integration procedure. Consequently, the present Z_{eff} results are not interpreted as conclusions derived under such a narrow error likelihood. The broadening prescription employed here should therefore be regarded as a conservative treatment, since it reduces the excessive statistical penalty associated with a single direction in the three dimensional compressed likelihood of the scalar amplitude. This approach is more consistent with the methodological scope of the present analysis, which does not yet incorporate a full CMB likelihood framework.

For a given power p , the effective Bayesian evidence is defined as:

$$Z_{\text{eff}}^{(A_s, n_s, r)}(p) = \int_{\Theta_p} \mathcal{L}_{\text{obs}}(\theta|p) \pi(\theta|p) d\theta, \quad (38)$$

where Θ_p denotes the prior parameter region associated with the model of monomial power p , while θ includes the parameters λ_p , C_ϕ , the initial field value, and the scaling factors specifying the initial inflaton velocity and radiation density. The function $\pi(\theta|p)$ represents the normalized prior density [52, 53]. Although Eq. (38) possesses the same integral structure as the standard Bayesian evidence, it is constructed using the observable likelihood \mathcal{L}_{obs} defined in this work. For this reason, it is referred to as the “effective Bayesian evidence under the observable likelihood,” and is abbreviated in the following discussion simply as the “effective evidence.” Physically, this quantity represents a prior weighted average over the entire allowed parameter region of the model with power p , measuring the extent to which the model can simultaneously satisfy the observational constraints on A_s , n_s , and $r_{0.05}$, together with the consistency conditions required for the warm inflation background. The quantity $\ln Z_{\text{eff}}$ therefore reflects both the likelihood value attained near the best fit region and the effective volume of high likelihood trajectories in parameter space. If compatibility with the observables can only be achieved within a highly restricted region of parameter space, the corresponding $Z_{\text{eff}}^{(A_s, n_s, r)}$ receives a prior volume penalty even when the best fit point itself remains acceptable. Conversely, if an extended parameter region is capable of maintaining a consistently high likelihood, a larger value of $Z_{\text{eff}}^{(A_s, n_s, r)}$ is obtained. The relative evidence difference is defined as

$$\Delta \ln Z_{\text{eff}}^{(A_s, n_s, r)}(p) = \ln Z_{\text{eff}}^{(A_s, n_s, r)}(p) - \ln Z_{\text{eff}}^{(A_s, n_s, r)}(p = 4). \quad (39)$$

If $\Delta Z_{\text{eff}}^{(A_s, n_s, r)} < 0$, the corresponding model receives a smaller prior averaged likelihood weight relative to the quartic potential. A larger absolute value of $\Delta Z_{\text{eff}}^{(A_s, n_s, r)}$ therefore indicates a more significant relative statistical disadvantage.

4. Numerical Strategy, Prior Settings, and Evidence Calculation

4.1. Computational Procedure

The statistical analysis proceeds as follows. First, three classes of monomial potentials with $p = 2, 3, 4$ are specified within the fixed low temperature dissipative framework $\Upsilon = C_\phi T^3 / \phi^2$. For each monomial power, parameter samples are then generated within the corresponding structure conditioned prior region, and the warm inflation background equations including radiation backreaction are solved numerically for every sampled parameter point. Trajectories that fail to generate a sufficient number of inflationary e-folds, or that violate basic physical requirements such as positive radiation density, $T_*/H_* > 1$, finite Q , or finite observable quantities, are assigned an extremely small likelihood, thereby rendering their contribution to the subsequent evidence integration negligible. For physically acceptable trajectories, the quantities \mathcal{P}_R , \mathcal{P}_T , n_s , and $r_{0.05}$ are evaluated at the pivot scale, and the broadened compressed observable likelihood is constructed from the observable set $(A_s, n_s, r_{0.05})$.

The genetic algorithm (GA) is employed solely to identify viable high likelihood regions within a fixed prior domain and to generate candidate points corresponding to the representative trajectories listed in Tab. 3. These candidate solutions are subsequently reevaluated using the same background evolution, primordial spectrum calculation, and likelihood pipeline. The final model ranking is not determined by the GA itself, but rather by the effective evidence Z_{eff} , which is computed using the `dynesty` (nested-sampling package) nested sampler within the same fixed prior region. Extended Markov Chain Monte Carlo (MCMC) chains are additionally used to verify the convergence of the principal posterior regions and the stability of the sampling procedure. Finally, the robustness of the hierarchy among the cases $p = 2, 3, 4$ is examined through variations of N_* , prior ranges, random seeds, and the treatment of the observational upper bound on r , together with tests involving the treatment of the primordial spectral components and the validity of the background trajectories.

Table 3: Representative high likelihood points used for illustration and trajectory diagnostics in the main results. The candidate points are obtained from broad range exploration and GA localization of high likelihood regions, and are re-examined by the unified background, primordial spectrum, and compressed likelihood calculations. All quantities are computed at the same pivot scale background point; the deviation of A_s from the observational central value should be understood under the broadened compressed likelihood of Tab. 2.

Model	n_s	$r_{0.05}$	A_s	Q_*	T_*/H_*	χ^2
$p = 2$	0.996616	0.047617	3.331×10^{-9}	6.19×10^{-4}	4.442	95.698
$p = 3$	0.977578	0.030739	2.306×10^{-9}	2.93×10^{-3}	8.509	10.482
$p = 4$	0.964201	0.026627	1.911×10^{-9}	4.68×10^{-3}	10.670	1.415

4.2. Parameter Space and Structural Conditional Prior

For each p , the sampled parameters are

$$\theta = (\log_{10} \lambda_p, \log_{10} C_\phi, \phi_0, \log_{10} f_\dot{\phi}, \log_{10} f_{\rho_R}). \quad (40)$$

The initial velocity and initial radiation density are written as

$$\dot{\phi}_0 = 10^{\log_{10} f_\dot{\phi}} \dot{\phi}_{\text{sr}}, \quad \rho_{R,0} = 10^{\log_{10} f_{\rho_R}} V(\phi_0), \quad (41)$$

where $\dot{\phi}_{\text{sr}} = -V_{,\phi}/(3H + \Upsilon)$. The reference prior A is shown in Tab. 4; the two additional prior sets used for sensitivity testing are given in Appendix A.

Table 4: Reference prior A based on the viable region. All priors are uniform distributions over the variables listed in the table. The ranges for different p reflect the scales of the viable warm branches identified during the preceding broad range exploration, rather than artificially imposed wide hyperpriors of uniform width.

Model	$\log_{10} \lambda_p$	$\log_{10} C_\phi$	ϕ_0	$\log_{10} f_\dot{\phi}$	$\log_{10} f_{\rho_R}$
$p = 2$	[-12.30,-9.20]	[5.00,9.40]	[12.0,38.0]	[-1.50,0.10]	[-14.0,-7.0]
$p = 3$	[-13.30,-10.00]	[5.60,9.60]	[18.0,42.0]	[-1.40,0.10]	[-14.0,-7.0]
$p = 4$	[-13.90,-12.60]	[6.40,8.70]	[30.0,42.0]	[-1.50,-0.30]	[-14.0,-8.5]

Reference prior A is not constructed through posterior shrinkage around an isolated best fit point. Instead, an initially broad parameter region is explored, and the GA is employed as a gradient free global search method to identify the principal warm inflation branches associated with each monomial power that simultaneously satisfy the requirements of sufficient inflationary e-folds, $T_*/H_* > 1$, positive radiation density, and finite observable likelihoods. Reference prior A is subsequently defined on the basis of this global exploration. The two additional prior choices, labeled B and C and listed in Appendix A, are introduced to examine the stability of the resulting hierarchy within this class of structure conditioned priors. All effective evidence values are obtained by integrating the normalized prior density over the corresponding fixed prior region. The role of the GA is therefore restricted to locating viable and high likelihood regions in parameter space, and it is not used as a replacement for posterior sampling or evidence integration.

From the standpoint of Bayesian model comparison, enforcing identical coordinate widths for ϕ_0 , C_ϕ , or λ_p across the cases $p = 2, 3, 4$ does not necessarily correspond to a physically fairer prior specification. This is primarily because the mass dimension of λ_p depends explicitly on the monomial power p , while the viable warm inflation branches associated with different powers naturally occupy distinct regions of parameter space and characteristic parameter scales. Consequently, complete uniformity of coordinate widths is not adopted here as the sole criterion for prior fairness. Instead, the fairness criterion for the structure conditioned priors is defined by whether the principal viable warm inflation branch corresponding to each monomial power is adequately covered within the prior region.

Table 5: Prior box width diagnostics for reference prior A. $\ln V_{\text{box}}$ is only used to display the difference in prior ranges; the evidence integration uses the normalized prior density.

Model	$\Delta \log_{10} \lambda_p$	$\Delta \log_{10} C_\phi$	$\Delta \phi_0$	$\Delta \log_{10} f_\dot{\phi}$	$\Delta \log_{10} f_{\rho_R}$	$\ln V_{\text{box}}$
$p = 2$	3.10	4.40	26.0	1.60	7.00	8.287
$p = 3$	3.30	4.00	24.0	1.50	7.00	8.110
$p = 4$	1.30	2.30	12.0	1.20	5.50	5.467

Tab. 5 is intended only to illustrate that the coordinate space prior volumes differ among the models under the chosen parameterization. Since Eq. (38) is constructed using a normalized prior density, the resulting evidence reflects the prior averaged likelihood within the corresponding structure conditioned prior region, rather than the raw number of high likelihood samples or the fitness values obtained from the GA search. To examine the dependence of the results on the prior specification, three prior sets, labeled A, B, and C, are explicitly tested in this work. Prior A is designed to cover the principal viable branch identified through the preceding broad

parameter exploration, prior B imposes partially unified widths for several auxiliary parameters, and prior C further enlarges the parameter ranges. If the evidence hierarchy were present only for prior A but disappeared under priors B and C, the resulting ordering could not be regarded as robust. As demonstrated in Sec. 5.2, the quartic potential remains the highest ranked case under all three prior choices, although the absolute magnitude of the evidence differences varies with the adopted prior region. The conclusion should therefore be interpreted as indicating that the ranking hierarchy remains stable within the present family of structure conditioned priors.

4.3. Global Search, Posterior Diagnostics, and Evidence Integration

Because the warm inflation background equations couple the quantities T , Q , ρ_R , and H in a highly nonlinear manner, the associated parameter space contains numerous invalid trajectories together with relatively narrow viable regions. In order to avoid inefficient exploration of large low likelihood regions during posterior sampling, a GA is first employed as a gradient free global search method [54, 55]. Within the prior ranges specified in Tab. 4, the GA is used to identify high likelihood regions that simultaneously satisfy the requirements of sufficient inflationary e-folds, $T_*/H_* > 1$, positive radiation density, and finite observable likelihoods. This global search procedure is used exclusively for locating viable and high likelihood regions in parameter space, and is not intended to replace posterior sampling or evidence integration.

Each parameter sample corresponds to the five dimensional parameter vector defined in Eq. (40). The associated likelihood weight is determined by Eq. (37), while trajectories failing to satisfy the basic physical requirements are assigned an extremely small likelihood value. The broad parameter exploration together with the identification of viable warm inflation branches provides the basis for selecting the prior region, but does not itself constitute the evidence integration procedure. Within the evidence calculation, the GA functions solely as a gradient free global search tool for locating viable high likelihood regions and for supplying suitable initial regions for posterior sampling; the prior domains specified in Tab. 4 and Appendix A remain fixed throughout the analysis. The effective evidence integration is then performed over the corresponding fixed prior region using the normalized prior density. Consequently, if a realization were integrated only within a local neighborhood identified by the optimization algorithm, the resulting quantity could at most be interpreted as a local marginal likelihood, rather than the effective evidence Z_{eff} defined in this work. All evidence values reported in this paper are therefore defined consistently with respect to the adopted fixed prior regions.

The posterior distribution is obtained primarily through the affine invariant ensemble MCMC method [56, 57], while the effective evidence is evaluated using nested sampling. The formal evidence calculation is performed with the `dynesty` nested-sampling package. In the principal analysis, $N_{\text{live}} = 500$ live points are used; the bounding strategy is set to the multi-ellipsoid option (`bound=multi`), the internal proposal is based on random walks (`sample=rwalk`), and the run is terminated when the remaining evidence estimate satisfies $d \ln Z = 0.05$. The prior transform maps the unit hypercube linearly onto the uniform prior intervals listed in the corresponding tables. Consequently, all parameter samples generated through the prior transform remain confined within the fixed prior region, and for every sampled point the background evolution and observable likelihood are recomputed independently. If a sampled parameter point fails to produce a finite background solution, cannot generate a sufficient number of inflationary e-folds, or does not yield finite values for A_s , n_s , and $r_{0.05}$, an extremely small log-likelihood is

assigned such that its contribution to the evidence integral becomes negligible. This procedure is equivalent to imposing a physical feasibility penalty on invalid trajectories within the same fixed prior domain, rather than applying a post hoc truncation of the prior volume.

The internal uncertainty of the evidence integration reported by `dynesty` is listed later in the effective evidence results table under the column labeled “numerical integration error,” while the scatter associated with independent random seeds is examined separately in Sec. 5.2. The normalizing flow posterior reconstruction is employed solely as an independent consistency check, intended to verify whether the principal posterior regions agree with both the MCMC posterior samples and the weighted posterior samples obtained from `dynesty` nested sampling. It does not contribute to the effective evidence calculation or to the final model ranking. The posterior overlap plot for the quartic potential displayed in Fig. 4 contains three classes of posterior diagnostic samples: MCMC posterior samples, weighted posterior samples from `dynesty` nested sampling, and posterior reconstruction samples generated by the normalizing flow. The purpose of this figure is exclusively to examine whether the dominant high likelihood regions identified by different posterior estimation methods remain mutually consistent in the $n_s - r_{0.05}$ plane. It is not used to modify the representative high likelihood points, the effective evidence values, or the potential hierarchy reported later in this work. The MCMC posterior diagnostics are summarized in Tab. 6. The results obtained from three independent random seed realizations demonstrate that the evidence ordering remains unchanged, indicating that the associated sampling scatter does not affect the principal model hierarchy conclusion of this analysis.

Table 6: Conservative long chain MCMC convergence diagnostics. τ_{int} is the integrated autocorrelation time, ESS is the effective sample size, and split- \hat{R} is the split-chain convergence diagnostic; the closer \hat{R} is to 1, the better the between chain agreement.

Model	Number of walkers	Number of steps	Mean acceptance fraction	$\max \tau_{\text{int}}$	Minimum ESS	Maximum split- \hat{R}
$p = 2$	80	25000	0.405	114.3	17500	1.0056
$p = 3$	80	25000	0.398	116.1	17228	1.0050
$p = 4$	80	25000	0.382	125.5	15934	1.0057

5. Numerical Results and Robustness Analysis

This section is devoted primarily to the presentation of the numerical results and robustness analyses, while the underlying physical interpretation and the range of applicability are deferred to Sec. 6. Five aspects are examined in sequence. First, the displacement of the three monomial potentials in the $n_s - r_{0.05}$ plane relative to the corresponding cold inflation benchmark is analyzed. Second, it is investigated whether the effective evidence continues to favor the same hierarchy once prior volume effects are incorporated. Third, the stability of this hierarchy is tested under variations of N_* , prior ranges, independent random seeds, and the treatment of the observational upper bound on r . Fourth, the influence of standard numerical settings entering the primordial spectrum calculation on the resulting observables is examined. Fifth, the representative trajectories are tested against the warm inflation, low temperature, and radiation subdominant conditions throughout the CMB window. Unless otherwise specified, the results presented in this section correspond to the reference choice $\sigma_r = 0.005$. The quantity Z_{eff} discussed throughout this work refers to the prior integral defined using the effective observable likelihood together with the adopted family of structure conditioned priors constructed from the viable warm inflation region.

5.1. Representative high likelihood Trajectories and the $n_s - r_{0.05}$ Plane

Tab. 3 lists representative high likelihood parameter points for the three monomial models, which are used for illustration, trajectory diagnostics, and stability tests of the primordial spectrum components. These parameter points are obtained through broad parameter exploration within reference prior A together with global localization using the GA. The GA is employed to identify candidate high likelihood regions that simultaneously satisfy the warm inflation conditions and the observational constraints, after which the parameter values reported in the table are reevaluated using the unified computational pipeline consisting of the background evolution, primordial spectrum calculation, and compressed observable likelihood. The table should not be interpreted as representing the effective evidence integration result or the posterior mean. Its purpose is instead to display the characteristic observational positions and microphysical properties associated with the three monomial cases within the same low temperature dissipative effective class.

Tab. 3 demonstrates that the quadratic potential simultaneously produces a blue tilted scalar spectral index together with an excessively large tensor amplitude, and therefore yields the largest value of χ^2 . In the cubic case, the tensor to scalar ratio $r_{0.05}$ is already reduced below the observational upper bound adopted in this work; however, the predicted value of n_s remains noticeably higher than the observational central value. By contrast, the quartic potential shifts n_s back toward the vicinity of the observed central value while still maintaining $r_{0.05} < 0.036$. These results indicate that the influence of warm scalar fluctuations on different monomial potentials does not correspond merely to a uniform overall displacement, but instead modifies the relative balance among the potential power, the spectral tilt, and the tensor amplitude.

Fig. 1 displays the locations of the analytic cold inflation reference points together with the representative warm inflation points in the $n_s - r_{0.05}$ plane. The cold inflation reference points are derived from the analytic relations given in Eq. (6) and are included solely to illustrate the tension imposed by the r constraint on low order monomial potentials; they are not incorporated into the effective evidence calculation. The representative warm inflation points are shifted collectively toward the lower- r region. In particular, the quartic potential moves from a location that clearly violates the r constraint in the cold inflation background to a region lying within the boundary allowed by the effective likelihood adopted in this work.

Based on Tab. 3 and Fig. 1, a preliminary conclusion may already be inferred at the level of representative parameter points: the quadratic potential exhibits the largest deviation from the preferred observational region, the cubic potential occupies an intermediate position, and the quartic potential provides the most favorable observational balance within the present low temperature dissipative framework. Nevertheless, a comparison based solely on isolated parameter points is insufficient to characterize the effective volume of the high likelihood region within the prior parameter space. In order to avoid identifying “a well fitting parameter point” with “a statistically favored model,” the analysis now proceeds to the effective Bayesian evidence.

5.2. Effective Evidence Ranking and Robustness Tests

Tab. 7 summarizes the effective evidence results obtained for $N_* = 55$, $\sigma_r = 0.005$, and reference prior A. The quantity $\ln Z_{\text{eff}}$ is evaluated using Eq. (38) and corresponds to the integral of the effective observable likelihood over the adopted prior region, while $\Delta \ln Z_{\text{eff}}$ denotes the evidence difference measured relative to the quartic potential.

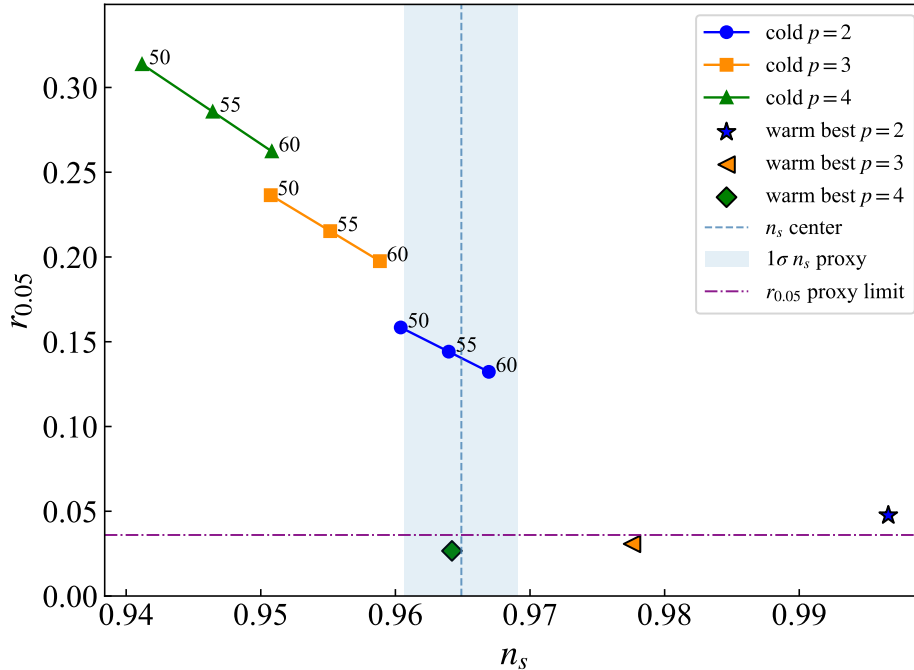


Figure 1: Positions of the cold inflation analytic reference points and the warm representative high likelihood points in the $n_s - r_{0.05}$ plane. The shaded band indicates the 1σ interval of n_s adopted in the broadened compressed likelihood of this paper; the horizontal dashed line indicates the r upper limit $r_{0.05} = 0.036$. The cold inflation points serve only as a reference and do not participate in the effective evidence integration.

Table 7: Effective evidence under $N_* = 55$ and reference prior A. $N_{\text{live}} = 500$; the numerical integration error is the internal uncertainty of $\ln Z_{\text{eff}}$ from a single nested sampling run.

Model	N_{live}	$\ln Z_{\text{eff}}$	Numerical integration error	$\Delta \ln Z_{\text{eff}}$
$p = 2$	500	-37.1116	0.1325	-32.1769
$p = 3$	500	-11.9207	0.1288	-6.9861
$p = 4$	500	-4.9347	0.1048	0

Tab. 7 yields the evidence hierarchy $p = 4 > p = 3 \gg p = 2$. Relative to the quartic potential, the cubic case gives $\Delta \ln Z_{\text{eff}} \simeq -6.99$, corresponding to a relative statistical weight of approximately $\exp(-6.99) \simeq 9.2 \times 10^{-4}$. For the quadratic potential, $\Delta \ln Z_{\text{eff}} \simeq -32.18$ is obtained, implying a much stronger suppression of the relative evidence weight. Since the numerical integration uncertainties for all three models are at the level of ~ 0.1 , these evidence differences are substantially larger than the intrinsic numerical error associated with a single nested sampling run. The effective evidence therefore captures not only the likelihood value attained near the best fit region, but also the effective parameter space volume capable of simultaneously satisfying the constraints on A_s , n_s , $r_{0.05}$, and the warm inflation consistency conditions. For this reason, it provides a more appropriate criterion for ranking different potentials within the same dissipative effective class than a comparison based solely on a single point χ^2 .

Tab. 8 examines the sensitivity of the evidence hierarchy to different discrete choices of N_* . For all three values considered, the quartic potential consistently remains the most favored case, the quadratic potential continues to be strongly disfavored, and the cubic potential occupies an intermediate position between the two.

Table 8: N_* discrete sensitivity test. The quartic potential serves as the zero point reference.

N_*	$\Delta \ln Z_{\text{eff}}(p = 2)$	$\Delta \ln Z_{\text{eff}}(p = 3)$	$\ln Z_{\text{eff}}(p = 4)$
50	-31.716	-5.005	-5.247
55	-32.177	-6.986	-4.935
60	-32.334	-8.090	-5.320

Tab. 9 investigates the dependence of the evidence hierarchy on the prior specification. As expected for Bayesian evidence, both the absolute evidence values and the corresponding evidence differences vary with the adopted prior volume. Nevertheless, the hierarchy $p = 4 > p = 3 > p = 2$ is preserved for all three prior choices. The essential issue is therefore not whether prior A imposes identical coordinate widths across the three monomial classes, but rather that none of the structure conditioned prior sets A, B, or C produces a reversal of the ranking. In particular, although the extended prior C reduces the relative evidence penalty associated with the quadratic potential when compared with the quartic case, the resulting value $\Delta \ln Z_{\text{eff}}(p = 2) = -11.36$ remains sufficiently negative that the principal conclusion is unchanged.

Table 9: Prior sensitivity test. The prior definitions are given in Appendix A. Prior A is the reference structural conditional prior calibrated by the viable region; the row for A uniformly adopts the main run results from Tab. 7. Priors B and C are used to test whether this ranking is stable under reasonable prior deformations.

Prior set	$\Delta \ln Z_{\text{eff}}(p = 2)$	$\Delta \ln Z_{\text{eff}}(p = 3)$	$\ln Z_{\text{eff}}(p = 4)$
A:Reference prior	-32.177	-6.986	-4.935
B:Unified auxiliary parameter widths	-31.628	-6.247	-5.665
C:Extended prior ranges	-11.361	-7.041	-6.371

To exclude the possibility that the observed hierarchy is an artifact of stochastic effects in the random search or evidence integration procedures, Tab. 10 reports the results obtained for $N_* = 55$ using three independent random seeds. All three realizations reproduce the same evidence ordering. The evidence difference between the cubic and quartic potentials remains stable within the range $\Delta \ln Z_{\text{eff}} \simeq -6.7$ to -7.0 , while the corresponding difference between the quadratic and quartic potentials consistently remains near $\Delta \ln Z_{\text{eff}} \simeq -32$.

Table 10: Stability of the effective evidence under independent random seeds. The table lists the evidence differences relative to the quartic potential for $N_* = 55$.

Random seed	$\Delta \ln Z_{\text{eff}}(p = 2)$	$\Delta \ln Z_{\text{eff}}(p = 3)$	$\ln Z_{\text{eff}}(p = 4)$
11	-32.177	-6.986	-4.935
22	-32.080	-6.761	-5.050
33	-32.105	-6.744	-5.092

Tab. 11 presents the sensitivity analysis associated with the treatment of the observational upper bound on r . As σ_r is varied from 0.003 to 0.010, the quartic potential consistently remains the model with the largest effective evidence. The evidence difference between the cubic and quartic potentials remains stable within the interval ~ 6.8 – 7.0 , while the quadratic potential continues to exhibit a strong evidence suppression relative to the quartic case. These results indicate that the statistical preference for the quartic potential is not an artifact of a particular smoothing prescription adopted near the upper bound on r .

Taken together, Tabs. 7–11 demonstrate that the quartic potential not only remains closer

Table 11: Sensitivity test on the treatment of the r upper bound. The quantity varied in the table is the smoothness width σ_r of the one sided penalty; the remaining settings adopt $N_* = 55$, and the quartic potential serves as the zero point reference.

σ_r	$\Delta \ln Z_{\text{eff}}(p = 2)$	$\Delta \ln Z_{\text{eff}}(p = 3)$	$\ln Z_{\text{eff}}(p = 4)$
0.003	-32.698	-6.840	-4.985
0.005	-32.177	-6.986	-4.935
0.010	-31.637	-6.889	-4.818

to the observational central values at the level of representative parameter points, but also consistently possesses the largest effective evidence in the prior averaged sense. Furthermore, this hierarchy is shown to remain stable under variations of N_* , prior volume, independent random seeds, and the treatment adopted for the observational upper bound on r .

5.3. Primordial Spectrum Calculation Stability and Low Temperature Trajectory Validity

Tab. 12 summarizes the impact of modifications in the primordial spectrum calculation settings on the predicted observables. The routine variations considered include changes in the finite difference step size together with $\pm 10\%$ variations in the strength of the growth factor $G(Q)$. The rightmost column reports the shifts relative to the baseline spectrum obtained after imposing $n_* = 0$, corresponding to the removal of the Bose Einstein thermal occupation contribution. The former variations constitute stability tests associated with standard numerical settings and with the fitting prescription adopted for the growth factor. By contrast, the latter modification changes the physical content of the warm inflation perturbation spectrum itself, since it corresponds to the limiting case in which the inflaton fluctuations fail to acquire thermal occupation. Consequently, this modification should not be interpreted as an ordinary numerical uncertainty.

Table 12: Stability of the primordial spectrum calculation and thermal occupation hypothesis test. Routine variations include changes in the finite difference step size and $\pm 10\%$ adjustments to the strength of $G(Q)$; the right column gives the changes relative to the baseline result when setting $n_* = 0$, i.e., removing the Bose Einstein thermal occupation number. This column is not an ordinary numerical stability test, but is used to characterize the extreme case in which inflaton fluctuations have not acquired thermal occupation.

Model	Maximum routine variation			Occupation number removed		
	$ \Delta n_s $	$ \Delta r $	$ \Delta \ln(10^{10} A_s) $	$ \Delta n_s $	$ \Delta r $	$ \Delta \ln(10^{10} A_s) $
$p = 2$	3.81×10^{-7}	1.35×10^{-8}	2.84×10^{-7}	0.098	0.371	2.173
$p = 3$	2.76×10^{-6}	1.80×10^{-7}	5.86×10^{-6}	0.0458	0.427	2.700
$p = 4$	5.13×10^{-6}	3.88×10^{-7}	1.46×10^{-5}	0.0155	0.413	2.805

Tab. 12 demonstrates that the variations in n_s and r induced by routine changes in the numerical settings remain substantially smaller than the intrinsic differences among the models, and therefore do not modify the effective evidence hierarchy. By contrast, imposing $n_* = 0$, corresponding to the removal of the Bose Einstein thermal occupation contribution, leads to a significant reduction in the scalar spectrum amplitude and increases the tensor to scalar ratio to $r \sim \mathcal{O}(0.4)$. This test represents the limiting scenario in which the inflaton fluctuations fail to acquire thermal occupation, rather than a small numerical perturbation of the baseline spectrum calculation. The result indicates that, within the present weak dissipation CMB window, the

principal mechanism responsible for suppressing the tensor amplitude is the enhancement of the warm scalar fluctuations by the thermal occupation number, rather than a large amplification produced by the dissipative growth factor. Consequently, the thermal occupation assumption constitutes a crucial physical prerequisite underlying the recovery mechanism of the quartic potential in the present analysis.

The trajectory level validity of the low temperature description is illustrated in Tab. 13, Fig. 2, and Fig. 3. The CMB window is defined by the interval $50 \leq N_{\text{to end}} \leq 60$. The table additionally reports the relevant dynamical quantities evaluated at the pivot scale, throughout the CMB window, and during the final few e-folds preceding the end of inflation, thereby allowing the perturbation generation stage to be distinguished from the inflation exit stage.

Table 13: Windowed microphysical diagnostics. The CMB window is defined as $50 \leq N_{\text{to end}} \leq 60$; the last 5 e-folds are only used to illustrate the radiation enhancement before exiting inflation and are not taken as an exclusion criterion.

Model	Window	T/H range	$\max Q$	$\max(\rho_R/V)$	$\max(T/\phi)$	$\max \epsilon_H$
$p = 2$	pivot	4.42–4.42	6.08×10^{-4}	7.9×10^{-6}	1.4×10^{-5}	0.027
$p = 2$	CMB window	2.82–7.87	3.45×10^{-3}	5.7×10^{-5}	2.6×10^{-5}	0.036
$p = 3$	pivot	8.55–8.55	2.97×10^{-3}	4.7×10^{-5}	1.4×10^{-5}	0.033
$p = 3$	CMB window	5.84–13.58	1.05×10^{-2}	2.1×10^{-4}	2.1×10^{-5}	0.042
$p = 4$	pivot	10.71–10.71	4.73×10^{-3}	8.4×10^{-5}	1.2×10^{-5}	0.036
$p = 4$	CMB window	7.72–15.48	1.18×10^{-2}	2.5×10^{-4}	1.5×10^{-5}	0.044
$p = 4$	Last 5 e-folds	2.77×10^3 – 1.81×10^4	8.71×10^2	0.999	1.2×10^{-4}	1.000

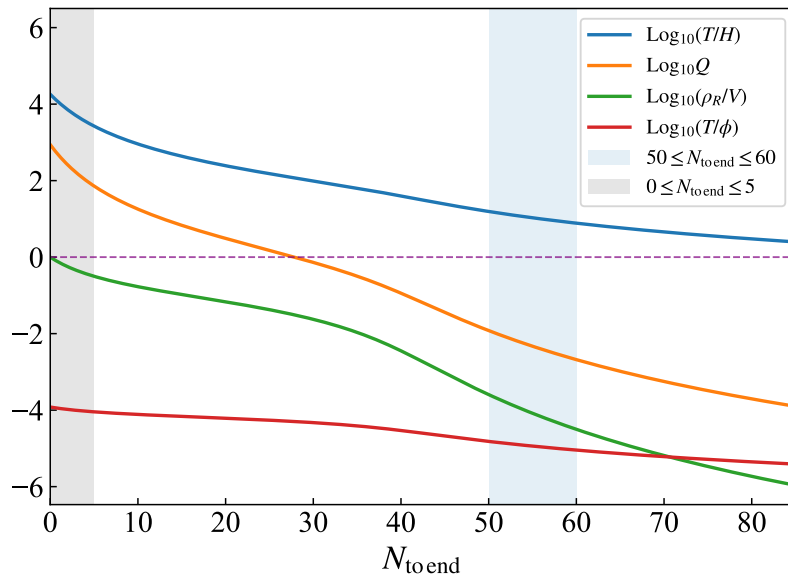


Figure 2: Validity diagnostics for the representative trajectory of the quartic potential. The horizontal axis shows the number of e-folds remaining until the end of inflation, $N_{\text{to end}}$; the light blue shaded region for $50 \leq N_{\text{to end}} \leq 60$ indicates the CMB perturbation generation window, the grey shaded region for $0 \leq N_{\text{to end}} \leq 5$ indicates the late time radiation enhanced stage, and the dotted vertical line marks the reference pivot position.

Tab. 13 demonstrates that all three models satisfy the condition $T/H > 1$ throughout the CMB window, while both Q and ρ_R/V remain small. For the quartic potential, the maximum values attained within the CMB window are approximately $Q \simeq 1.18 \times 10^{-2}$ and $\rho_R/V \simeq 2.5 \times 10^{-4}$, corresponding to a warm inflation regime characterized by weak dissipation and subdominant radiation. The validity of the low temperature expansion is controlled by the

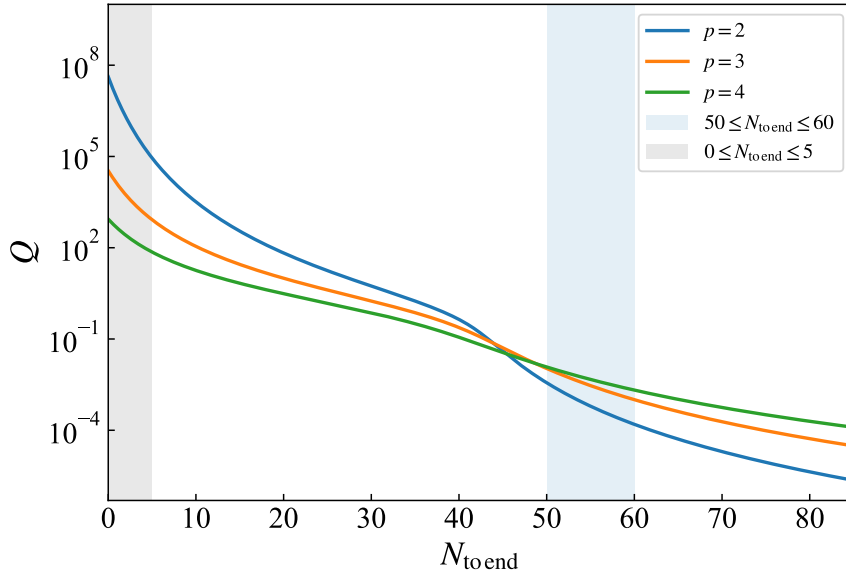


Figure 3: Evolution of the dissipation ratio Q for the three representative trajectories. The light blue shaded region indicates the CMB perturbation generation window, and the grey shaded region indicates the late time radiation enhanced stage. In the CMB window $Q \ll 1$, and both radiation and dissipation increase rapidly in the last few e-folds.

requirement $T/m_\chi < 1$. If the heavy mediator mass is parameterized as $m_\chi = g_\chi \phi$, the values of T/ϕ listed in the table provide a conservative lower bound on the coupling g_χ . Within the CMB window, the characteristic ratio $T/\phi \sim 10^{-5}$ is obtained, indicating that the low temperature expansion can be maintained without requiring non-perturbative couplings. Combined with the typical value $T/H \sim 10$, this implies $\phi/H \sim 10^6$, such that the ratio $m_\chi/H = g_\chi \phi/H$ can remain far larger than unity over a broad range of g_χ . This property ensures that, within the low temperature two stage framework, the heavy mediator may consistently remain heavier than both the thermal bath temperature and the Hubble scale.

It should further be noted that during the final few e-folds of inflation, the ratio ρ_R/V increases rapidly and can approach unity. This behavior should not be interpreted as an instability of the CMB perturbation calculation, but rather as a natural consequence of the termination of inflation and the associated energy transfer stage. Accordingly, the condition $\rho_R/V < 0.5$ over the entire trajectory up to $\epsilon_H = 1$ is not imposed here as a strict exclusion criterion. Instead, the criterion adopted in this work requires radiation to remain subdominant throughout the CMB window and at the pivot scale, while allowing the late time evolution to enter a radiation enhanced regime near the end of inflation.

Fig. 4 demonstrates that the three sets of posterior diagnostic samples overlap within the principal high likelihood region and collectively cover the $n_s - r_{0.05}$ region surrounding the representative quartic potential point listed in Tab. 3. This agreement indicates that the dominant high likelihood regions identified through MCMC posterior sampling, weighted nested sampling posterior samples, and the normalizing flow posterior reconstruction remain mutually consistent. When combined with the convergence diagnostics reported in Tab. 6, namely $\hat{R} < 1.01$, chain lengths exceeding $50\tau_{\text{int}}$, and an effective sample size satisfying $\text{ESS} > 1.5 \times 10^4$, no significant evidence of posterior non-convergence is observed.

Based on the preceding results, the model hierarchy obtained in this analysis may be summarized as follows: within the low temperature dissipative framework characterized by

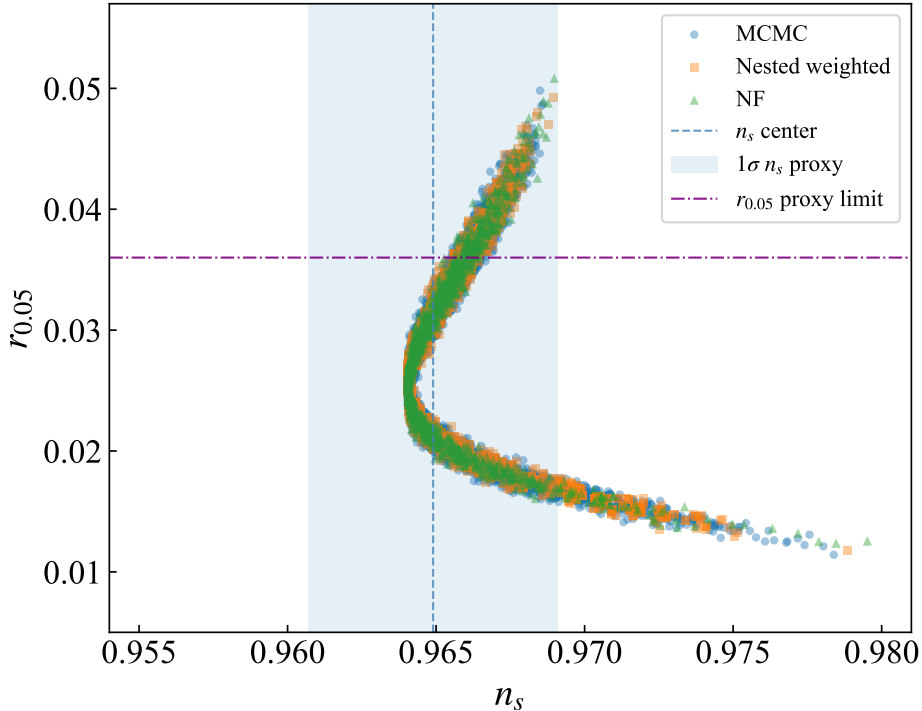


Figure 4: Overlap of the posterior regions for the quartic potential branch in the $n_s - r_{0.05}$ plane. Blue, orange, and green points represent MCMC posterior samples, dynesty nested sampling weighted posterior samples, and normalizing flow posterior reconstruction samples, respectively. The vertical dashed line indicates $n_s = 0.9649$, and the horizontal dashed line indicates the tensor upper limit $r_{0.05} = 0.036$. This figure is used to check whether the main high likelihood regions identified by different posterior estimation methods are consistent.

$\Upsilon = C_\phi T^3 / \phi^2$, under the effective observable likelihood adopted here, and within the family of structure conditioned priors constructed from the viable warm inflation region, the quartic potential receives the largest prior averaged likelihood weight, the cubic potential occupies an intermediate position, and the quadratic potential is clearly disfavored. The resulting conclusion should therefore be interpreted as an “effective evidence preference within a fixed low temperature dissipative effective class and a specified family of structure conditioned priors.” The large values $C_\phi \sim 10^6 - 10^7$ should furthermore be interpreted as effective dissipative strengths enhanced by multiple degrees of freedom or composite dissipative sectors, rather than as individual fundamental coupling constants.

6. Physical Discussion

6.1. Physical mechanism favoring the quartic potential

For cold monomial inflationary potentials, the principal difficulty associated with the quartic case originates from an excessively large tensor to scalar ratio together with a relatively low spectral index. Within the low temperature warm inflation background, this conclusion is not modified through a simple uniform displacement of all models, but rather through a change in the denominator of $r = \mathcal{P}_T / \mathcal{P}_\mathcal{R}$ induced by the enhancement of thermal scalar fluctuations. At the representative quartic potential point considered in this work, the dissipation strength satisfies $Q_* \simeq 4.7 \times 10^{-3}$, placing the system within the weak dissipation regime. Consequently, the dissipative growth factor $G(Q)$ does not provide the dominant contribution. Instead, the

crucial effect arises from the Bose Einstein thermal occupation term associated with the condition $T_*/H_* > 1$. This physical mechanism explains why the quartic potential can achieve a more favorable balance between n_s and r in the warm inflation framework, whereas it experiences the strongest tension with the r constraint in the cold inflation limit.

The same physical interpretation also delineates the domain of applicability of the present conclusions. If the inflaton fluctuations are not efficiently thermalized, or if the thermal occupation number remains substantially below the Bose Einstein limit, the enhancement of the scalar spectrum would be significantly reduced, and the corresponding recovery mechanism for the quartic potential would become much weaker. The extreme thermal occupation test obtained by imposing $n_* = 0$ in Tab. 12 is specifically designed to illustrate this feature. The conclusions presented in this work therefore apply only to the low temperature warm inflation branch in which the thermal occupation assumption is valid, and should not be interpreted as implying that “warm inflation generically favors the quartic potential.”

6.2. Statistical meaning of the effective evidence

The quantity $Z_{\text{eff}}^{(A_s, n_s, r)}$ represents the prior averaged likelihood evaluated under the broadened compressed observable likelihood adopted in this work. Although it possesses the mathematical structure of a Bayesian evidence, it should be distinguished from the model evidence derived from a full CMB likelihood analysis. Its primary utility lies in providing a controlled, reproducible, and computationally efficient framework for model comparison. Within this framework, all monomial potentials are evaluated using the same warm inflation background equations, the same primordial spectrum calculation procedure, the same compressed observable likelihood, and the same family of structure conditioned priors.

The results presented here are therefore more appropriately interpreted as an effective ranking of low temperature warm monomial potentials, rather than as a definitive conclusion derived from a full observational data analysis. More precisely, within the framework defined by the fixed low temperature dissipative form $\Upsilon = C_\phi T^3/\phi^2$, the broadened compressed observable likelihood, and the family of structure conditioned priors constructed through broad parameter exploration and identification of the viable warm inflation branches, the quartic monomial potential achieves the highest effective evidence among the three low order effective potentials with $p = 2, 3, 4$. Furthermore, this hierarchy is found to remain stable under variations of N_* , the prior family, independent random seeds, and the treatment adopted for the observational upper bound on r . The principal physical mechanism responsible for the recovery of the quartic potential is not strong dissipative friction, but rather the enhancement of the scalar spectrum by the thermal occupation contribution within the weak dissipation warm inflation regime characterized by $Q_* \ll 1$ and $T_*/H_* > 1$, which in turn reduces the tensor to scalar ratio r .

6.3. Prior Fairness and Microphysical Cost

The effective evidence necessarily depends on the adopted prior region. The reference prior A employed in this work is constructed as a structure conditioned prior obtained through broad parameter exploration and identification of the viable warm inflation branches, rather than through the imposition of an artificially enlarged common parameter box designed to enforce identical coordinate widths for all three model classes. Requiring different monomial potentials to share the same parameter widths in ϕ_0 or $\log C_\phi$ should not automatically be regarded as a

fairer prescription, since both the mass dimension of λ_p and the characteristic scale of the viable warm branch vary with the monomial power p . The central issue addressed here is therefore the following: once the principal viable branch associated with each value of p is adequately covered, does the evidence hierarchy remain stable under reasonable deformations of the prior region? The three prior choices together with the explicit prior width tables demonstrate that the principal evidence hierarchy remains stable within the present family of priors calibrated according to the viable warm inflation region.

From the microphysical perspective, the requirement $C_\phi \sim 10^6\text{--}10^7$ constitutes the principal cost associated with the model realization considered in this work. Within the low temperature two stage dissipative framework, the coefficient C_ϕ is typically determined by a combination of the number of heavy mediator fields, the light thermal bath degrees of freedom, and the associated interaction couplings, and may often be summarized through a model dependent structure of the form $C_\phi \sim \mathcal{C} h^4 N_\chi N_y^2$, where h denotes a representative coupling strength, N_χ and N_y characterize the numbers of heavy mediator channels and light thermal bath channels, respectively, and \mathcal{C} represents a model dependent numerical coefficient. If the effective coupling remains of order $O(1)$, achieving values in the range $10^6\text{--}10^7$ generally requires $N_\chi N_y^2$, or an equivalent composite enhancement factor, to become very large. For smaller couplings, an even larger multiplicity of degrees of freedom or composite enhancement is required. At the same time, the quantities g_* and C_ϕ should not be directly identified with one another: g_* counts only the relativistic light degrees of freedom contained within the thermal bath, whereas C_ϕ may additionally encode the effects of integrated-out heavy mediators together with multi-channel dissipative structures. The conclusions presented in this work should therefore be interpreted specifically as demonstrating a stable effective evidence preference for the quartic potential within the low temperature dissipative effective class considered here.

7. Conclusion

Within the cold single field slow roll framework, the observational constraints on low order monomial potentials arise primarily from r . As the monomial power increases, the cold inflation background predicts larger values of r , thereby placing the quartic potential under strong tension with the current observational upper bound. Low temperature warm inflation introduces an alternative physical mechanism: the thermal bath does not directly amplify the tensor spectrum, but instead enhances the scalar spectrum through thermal occupation effects and dissipative perturbations, thereby modifying the correspondence between r and the potential power that is characteristic of the cold inflation scenario. Consequently, the r constraint problem for monomial potentials in the cold framework may be reformulated as the problem of comparing the effective evidence of different low order effective potentials within a fixed dissipative structure.

Within the unified low temperature dissipative framework characterized by $\Upsilon = C_\phi T^3/\phi^2$, three classes of monomial potentials, $V_p(\phi) = \lambda_p \phi^p/p$ with $p = 2, 3, 4$, are systematically compared. All three monomial branches are evaluated using the same warm inflation background equations, the same primordial spectrum calculation procedure, and the same broadened compressed observable likelihood. The introduction of the effective Bayesian evidence further promotes the comparison from isolated observationally viable parameter points to a hierarchy test among models within the adopted family of structure conditioned priors. This constitutes the principal feature distinguishing the present analysis from conventional single point comparisons

performed solely in the $n_s - r$ plane.

For the reference configuration defined by $N_* = 55$, $\sigma_r = 0.005$, and the structure conditioned prior constructed from the viable warm inflation branch, the quadratic and cubic potentials yield $\Delta \ln Z_{\text{eff}}(p = 2) = -32.18$ and $\Delta \ln Z_{\text{eff}}(p = 3) = -6.99$, respectively, relative to the quartic potential. This hierarchy is found to remain stable under variations of the discrete choices of N_* , deformations of the prior region, independent random seeds, and different treatments of the observational upper bound on r . Consequently, within the low temperature dissipative effective class and the compressed observable likelihood adopted in this work, the three low order monomial potentials exhibit a stable effective evidence hierarchy given by $p = 4 > p = 3 \gg p = 2$. This result indicates that the statistical advantage of the quartic potential does not arise from an isolated high likelihood parameter point, but rather from the combined prior averaged contribution of observational compatibility and viable parameter space volume.

The physical origin of the dominance of the quartic potential can be traced to a CMB window characterized by weak dissipation together with significant thermal occupation. The representative quartic potential branch satisfies the conditions $Q_* \ll 1$ and $T_*/H_* > 1$. Consequently, the reduction of r is not primarily driven by strong dissipative friction, but instead arises mainly from the enhancement of the scalar spectrum by the Bose Einstein thermal occupation number. An analysis of the individual contributions to the primordial spectrum further demonstrates that removing the thermal occupation term substantially weakens the scalar spectrum enhancement and drives r toward significantly larger values. The transition of the quartic potential from a r constrained scenario in the cold inflation framework to a high evidence branch in the warm inflation framework therefore depends crucially on this thermal occupation enhancement mechanism, rather than on the background friction effect associated with the strong dissipation regime.

The trajectory validity analysis demonstrates that, throughout the CMB window, the warm inflation condition, the weak dissipation condition, and the radiation subdominance condition are simultaneously satisfied and remain compatible with the requirements of the low temperature expansion. Near the end of inflation, the radiation energy fraction increases rapidly, corresponding to the onset of the inflation exit and energy transfer phase; this late time behavior does not affect the determination of the pivot scale perturbations. The distinction between these two stages indicates that the present high evidence branch belongs to a warm inflation regime characterized by low temperature, weak dissipation, and significant thermal occupation, rather than to a late time dynamical phase dominated by radiation.

The observational viability of monomial inflationary potentials is not determined solely by the monomial power within the cold inflation framework. Under the fixed low temperature dissipative form, the broadened compressed observable likelihood, and the present family of structure conditioned priors, the quartic potential attains the highest effective evidence among the cases $p = 2, 3, 4$. Consequently, the quartic monomial potential, which is excluded by the r constraint in the cold inflation picture, can be transformed into the most strongly supported low order branch through warm inflation dynamics enhanced by thermal occupation effects. The effective evidence hierarchy established here also provides a framework that can be generalized to future comparative studies involving different dissipative structures and broader classes of effective inflationary potentials.

Acknowledgements

This work was supported in part by the National Natural Science Foundation of China under Grant No. 12565014, by the Talent Research Startup Foundation of Hainan Normal University: HSZK-KYQD-202523, by Opening Foundation of Shanghai Key Laboratory of Particle Physics and Cosmology under Grant No. 22DZ2229013-5, by Hainan Provincial Natural Science Foundation of China under Grant No. 126MS0134, by Chongqing Natural Science Foundation project under Grant No. CSTB2022NSCQ-MSX0432, by Science and Technology Research Project of Chongqing Education Commission under Grant No. KJQN202200621 and No. KJQN202200650, and by Chongqing Human Resources and Social Security Administration Program under Grants No. D63012022005.

A. Structural Conditional Prior Ranges and Sensitivity Settings

This appendix summarizes the three prior sets denoted by A, B, and C, which are introduced to test the prior sensitivity and robustness of the effective evidence hierarchy. Reference prior A is not constructed as a local prior obtained through post hoc contraction around the GA best fit point. Instead, it is defined as a structure conditioned reference prior established after broad parameter exploration, screening for basic physical viability, and GA-assisted localization of the viable warm inflation branches; consequently, its parameter ranges are chosen to cover only the physically viable warm branches associated with each monomial model. Prior B is introduced in order to partially unify the interval widths of several auxiliary parameters across different monomial powers, thereby testing whether the evidence hierarchy is sensitive to moderate changes in the prior volume assignment. For the cases $p = 3$ and $p = 4$, the ranges of $\log_{10} C_\phi$, ϕ_0 , $\log_{10} f_\phi$, and $\log_{10} f_{\rho_R}$ are adjusted to satisfy the same interval width standard. For the $p = 2$ case, the corresponding widths in prior A already satisfy this requirement; therefore, prior B for $p = 2$ is kept identical to prior A. Prior C further enlarges the parameter ranges on the basis of prior A, in order to test whether the resulting evidence hierarchy remains stable under substantially broader prior boundaries. The purpose of introducing these three prior sets is not to demonstrate complete invariance of the evidence hierarchy under arbitrary prior choices, but rather to test whether the principal conclusions depend exclusively on a single excessively narrow or highly tuned prior region. All MCMC posterior analyses and nested sampling evidence calculations are performed within these fixed prior domains. The GA is used solely for locating viable and high likelihood regions in parameter space, and does not generate posterior samples or replace the evidence integration procedure.

Table 14: Priors A, B, and C. All entries are uniform intervals for the corresponding variables.

Prior set	Model	$\log_{10} \lambda_p$	$\log_{10} C_\phi$	ϕ_0	$\log_{10} f_{\dot{\phi}}$	$\log_{10} f_{\rho_R}$
A	$p = 2$	[-12.30,-9.20]	[5.00,9.40]	[12.0,38.0]	[-1.50,0.10]	[-14.0,-7.0]
A	$p = 3$	[-13.30,-10.00]	[5.60,9.60]	[18.0,42.0]	[-1.40,0.10]	[-14.0,-7.0]
A	$p = 4$	[-13.90,-12.60]	[6.40,8.70]	[30.0,42.0]	[-1.50,-0.30]	[-14.0,-8.5]
B	$p = 2$	[-12.30,-9.20]	[5.00,9.40]	[12.0,38.0]	[-1.50,0.10]	[-14.0,-7.0]
B	$p = 3$	[-13.30,-10.00]	[5.40,9.80]	[17.0,43.0]	[-1.45,0.15]	[-14.0,-7.0]
B	$p = 4$	[-13.90,-12.60]	[5.35,9.75]	[23.0,49.0]	[-1.70,-0.10]	[-14.75,-7.75]
C	$p = 2$	[-13.85,-7.65]	[2.80,11.60]	[1.0,51.0]	[-2.30,0.90]	[-17.5,-3.5]
C	$p = 3$	[-14.95,-8.35]	[3.60,11.60]	[6.0,54.0]	[-2.15,0.85]	[-17.5,-3.5]
C	$p = 4$	[-14.55,-11.95]	[5.25,9.85]	[24.0,48.0]	[-2.10,0.30]	[-16.75,-5.75]

References

- [1] A. H. Guth, “The Inflationary Universe: A Possible Solution to the Horizon and Flatness Problems,” *Phys. Rev. D* **23**, 347-356 (1981).
- [2] A. D. Linde, “A New Inflationary Universe Scenario: A Possible Solution of the Horizon, Flatness, Homogeneity, Isotropy and Primordial Monopole Problems,” *Phys. Lett. B* **108**, 389-393 (1982).
- [3] A. Albrecht and P. J. Steinhardt, “Cosmology for Grand Unified Theories with Radiatively Induced Symmetry Breaking,” *Phys. Rev. Lett.* **48**, 1220-1223 (1982).
- [4] D. H. Lyth and A. Riotto, “Particle physics models of inflation and the cosmological density perturbation,” *Phys. Rept.* **314**, 1-146 (1999).
- [5] D. Baumann, “Inflation,” [arXiv:0907.5424](https://arxiv.org/abs/0907.5424).
- [6] G. Tasinato, “An analytic approach to non-slow-roll inflation,” *Phys. Rev. D* **103**, no.2, 023535 (2021).
- [7] P. Adshead, C. P. Burgess, R. Holman and S. Shandera, “Power-counting during single-field slow-roll inflation,” *JCAP* **02**, 016 (2018).
- [8] H. S. Yuan, Z. Y. Peng and Y. S. Piao, “Single field slow-roll inflation with step uplift to $n_s = 1$,” [arXiv:2604.02823 \[astro-ph.CO\]](https://arxiv.org/abs/2604.02823).
- [9] D. Baumann, P. J. Steinhardt, K. Takahashi and K. Ichiki, “Gravitational Wave Spectrum Induced by Primordial Scalar Perturbations,” *Phys. Rev. D* **76**, 084019 (2007).
- [10] Y. Akrami *et al.* [Planck], “Planck 2018 results. X. Constraints on inflation,” *Astron. Astrophys.* **641**, A10 (2020).
- [11] P. A. R. Ade *et al.* [BICEP and Keck], “Improved Constraints on Primordial Gravitational Waves using Planck, WMAP, and BICEP/Keck Observations through the 2018 Observing Season,” *Phys. Rev. Lett.* **127**, no.15, 151301 (2021).
- [12] N. Aghanim *et al.* [Planck], “Planck 2018 results. I. Overview and the cosmological legacy of Planck,” *Astron. Astrophys.* **641**, A1 (2020).
- [13] H. Sheikahmadi, A. Mohammadi, A. Aghamohammadi, T. Harko, R. Herrera, C. Corda, A. Abebe and K. Saaidi, “Constraining chameleon field driven warm inflation with Planck 2018 data,” *Eur. Phys. J. C* **79**, no.12, 1038 (2019).
- [14] A. D. Linde, “Chaotic Inflation,” *Phys. Lett. B* **129**, 177-181 (1983).
- [15] K. Harigaya, M. Ibe, K. Schmitz and T. T. Yanagida, “Dynamical fractional chaotic inflation,” *Phys. Rev. D* **90**, no.12, 123524 (2014).
- [16] K. Rezazadeh, A. Abdolmaleki and K. Karami, “Power-law and intermediate inflationary models in $f(T)$ -gravity,” *JHEP* **01**, 131 (2016).
- [17] M. Shahalam, M. Sharma, Q. Wu and A. Wang, “Preinflationary dynamics in loop quantum cosmology: Power-law potentials,” *Phys. Rev. D* **96**, no.12, 123533 (2017).

- [18] G. Ballesteros and C. Tamarit, “Radiative plateau inflation,” [JHEP **02**, 153 \(2016\)](#).
- [19] S. Bartrum, M. Bastero-Gil, A. Berera, R. Cerezo, R. O. Ramos and J. G. Rosa, “The importance of being warm (during inflation),” [Phys. Lett. B **732**, 116-121 \(2014\)](#).
- [20] A. Berera, I. G. Moss and R. O. Ramos, “Warm Inflation and its Microphysical Basis,” [Rept. Prog. Phys. **72**, 026901 \(2009\)](#).
- [21] A. Berera, “The Warm Inflation Story,” [Universe **9**, no.6, 272 \(2023\)](#).
- [22] V. Kamali, M. Motaharfard and R. O. Ramos, “Recent Developments in Warm Inflation,” [Universe **9**, no.3, 124 \(2023\)](#).
- [23] L. M. H. Hall, I. G. Moss and A. Berera, “Scalar perturbation spectra from warm inflation,” [Phys. Rev. D **69**, 083525 \(2004\)](#).
- [24] C. Graham and I. G. Moss, “Density fluctuations from warm inflation,” [JCAP **07**, 013 \(2009\)](#).
- [25] R. O. Ramos and L. A. da Silva, “Power spectrum for inflation models with quantum and thermal noises,” [JCAP **03**, 032 \(2013\)](#).
- [26] G. Montefalcone, V. Aragam, L. Visinelli and K. Freese, “WarmSPy: a numerical study of cosmological perturbations in warm inflation,” [JCAP **01**, 032 \(2024\)](#).
- [27] T. Eadkhong, P. Dam-O, P. Channuie and D. Momeni, “Nonminimally-coupled warm Higgs inflation: Metric vs. Palatini formulations,” [Nucl. Phys. B **994**, 116289 \(2023\)](#).
- [28] J. Yuennan, R. Myrzakulov, P. K. Sahoo, F. Atamurotov and P. Channuie, “Minimal warm Higgs inflation in Palatini R^2 gravity,” [Eur. Phys. J. C **85**, no.9, 972 \(2025\)](#).
- [29] W. Cheng, X. W. Chen, R. Zhou, J. J. Jiang, X. R. Dai, Z. H. Zhang and T. Qin, “Exploring the impact of the dissipation coefficient in warm Higgs inflation,” [Phys. Rev. D **109**, no.8, 083509 \(2024\)](#).
- [30] I. G. Moss and C. Xiong, “Dissipation coefficients for supersymmetric inflatary models,” [arXiv:hep-ph/0603266](#).
- [31] M. Bastero-Gil and A. Berera, “Warm inflation dynamics in the low temperature regime,” [Phys. Rev. D **76**, 043515 \(2007\)](#).
- [32] M. Bastero-Gil and A. Berera, “Warm inflation model building,” [Int. J. Mod. Phys. A **24**, 2207-2240 \(2009\)](#).
- [33] M. Bastero-Gil, A. Berera, R. O. Ramos and J. G. Rosa, “General dissipation coefficient in low-temperature warm inflation,” [JCAP **01**, 016 \(2013\)](#).
- [34] M. Bastero-Gil, A. Berera, R. O. Ramos and J. G. Rosa, “Warm Little Inflaton,” [Phys. Rev. Lett. **117**, no.15, 151301 \(2016\)](#).
- [35] M. Bastero-Gil, A. Berera, R. Hernández-Jiménez and J. G. Rosa, “Warm inflation within a supersymmetric distributed mass model,” [Phys. Rev. D **99**, no.10, 103520 \(2019\)](#).

- [36] K. V. Berghaus, P. W. Graham and D. E. Kaplan, “Minimal Warm Inflation,” *JCAP* **03**, 034 (2020).
- [37] K. V. Berghaus, M. Drewes and S. Zell, “Warm Inflation with the Standard Model,” *Phys. Rev. Lett.* **135**, no.17, 171002 (2025).
- [38] S. Bartrum, A. Berera and J. G. Rosa, “Warming up for Planck,” *JCAP* **06**, 025 (2013).
- [39] M. Benetti and R. O. Ramos, “Warm inflation dissipative effects: predictions and constraints from the Planck data,” *Phys. Rev. D* **95**, no.2, 023517 (2017).
- [40] M. Bastero-Gil, S. Bhattacharya, K. Dutta and M. R. Gangopadhyay, “Constraining Warm Inflation with CMB data,” *JCAP* **02**, 054 (2018).
- [41] R. Arya, A. Dasgupta, G. Goswami, J. Prasad and R. Rangarajan, “Revisiting CMB constraints on warm inflation,” *JCAP* **02**, 043 (2018).
- [42] Y. Zhang, “Warm Inflation With A General Form Of The Dissipative Coefficient,” *JCAP* **03**, 023 (2009).
- [43] F. B. M. d. Santos, R. de Souza and J. S. Alcaniz, “A comparative analysis of dissipation coefficients in warm inflation,” *JCAP* **10**, 071 (2024).
- [44] W. Cheng, X. Peng, J. w. Zhang, R. Zhou and Y. Pan, “Comparison of Effective Dissipation Channels in Warm Higgs Inflation from Warm Background Evolution,” [arXiv:2604.17467](https://arxiv.org/abs/2604.17467).
- [45] L. Visinelli, “Observational Constraints on Monomial Warm Inflation,” *JCAP* **07**, 054 (2016).
- [46] G. Ballesteros, A. Perez Rodriguez and M. Pierre, “Monomial warm inflation revisited,” *JCAP* **03**, 003 (2024).
- [47] M. Laine, S. Procacci and A. Rogelj, “Evolution of coupled scalar perturbations through smooth reheating. Part II. Thermal fluctuation regime,” *JCAP* **12**, 058 (2025).
- [48] A. Ito and R. O. Ramos, “Warm multi-natural inflation,” *JCAP* **08**, 076 (2025).
- [49] F. B. M. d. Santos, R. Silva, S. S. da Costa, M. Benetti and J. S. Alcaniz, “Warm β -exponential inflation and the swampland conjectures,” *Eur. Phys. J. C* **83**, no.2, 178 (2023).
- [50] H. Prince and J. Dunkley, “Data compression in cosmology: A compressed likelihood for Planck data,” *Phys. Rev. D* **100**, no.8, 083502 (2019).
- [51] L. Balkenhol, “Compressed ‘CMB-lite’ Likelihoods Using Automatic Differentiation,” [arXiv:2412.00826](https://arxiv.org/abs/2412.00826).
- [52] J. Martin, C. Ringeval and V. Vennin, “Cosmic Inflation at the crossroads,” *JCAP* **07**, 087 (2024).
- [53] R. Easther and H. V. Peiris, “Bayesian Analysis of Inflation II: Model Selection and Constraints on Reheating,” *Phys. Rev. D* **85**, 103533 (2012).

- [54] W. Cheng, “Three channel dissipative warm Higgs inflation with global inference via genetic algorithms,” [arXiv:2512.23423](#).
- [55] R. C. Bernardo and Y. Chen, “Genetic algorithm demystified for cosmological parameter estimation,” *Astron. Comput.* **55**, 101041 (2026).
- [56] R. Allison and J. Dunkley, “Comparison of sampling techniques for Bayesian parameter estimation,” *Mon. Not. Roy. Astron. Soc.* **437**, no.4, 3918-3928 (2014).
- [57] D. Foreman-Mackey, D. W. Hogg, D. Lang and J. Goodman, “emcee: The MCMC Hammer,” *Publ. Astron. Soc. Pac.* **125**, 306-312 (2013).